International Journal of Environment, Agriculture and Biotechnology
Vol-11, Issue-5; Sep-Oct, 2026
Peer-Reviewed International Journal
Journal Home Page Available: https://ijeab.com/
Journal DOI: 10.22161/ijeab

Ring-like Expansion of Heat Islands and Fragmentation of Cold Islands: Remote Sensing-Based Monitoring and Driving Mechanisms of Thermal Environment Evolution in Wuhan

Anqi Bai, Xinrui Gao, Yuxi Yao, Jieting Zhang, Ruei-Yuan Wang*

School of Sciences, Guangdong University of Petrochem Technology (GDUPT), Maoming 525000, China

Received: 18 Sep 2026; Received in revised form: 16 Oct 2026; Accepted: 22 Oct 2026; Available online: 28 Oct 2026
©2026 The Author(s). Published by Infogain Publication. This is an open-access article *under* the CC BY license (https://creativecommons.org/licenses/by/4.0/).

Abstract— *The urban heat island (UHI) effect is a typical eco-environmental problem during urbanization, significantly affecting urban ecosystems and residents' quality of life. Using Wuhan City as the study area, we employed Landsat images from 2013, 2018, and 2024, along with multi-source data including DEM, population density, and land use types. Land surface temperature (LST) was retrieved using the mono-window algorithm. By combining the mean–standard deviation classification method with the geographical detector model, we systematically analyzed the spatiotemporal evolution characteristics and driving mechanisms of the UHI effect. The results show that: (1) From 2013 to 2024, the proportion of heat islands in Wuhan increased from 43.98% to 54.17%, while the proportion of cold islands decreased from 24.81% to 19.96%. Heat islands expanded outward in a concentric pattern with continuously increasing intensity, whereas cold islands shrank globally and their fragmentation intensified. (2) The spatial pattern exhibited a stable dual-circle structure of "strong heat islands in the center—shrinking cold islands in the periphery." The Yangtze River and Han River acted as natural "cold corridors," serving as spatial barriers that segmented heat islands. (3) The geographical detector revealed that NDBI and NDVI were the long-term dominant independent driving factors, and their interaction yielded the highest explanatory power ($q = 0.771$). The superimposed effect of construction land expansion and vegetation degradation constituted the core mechanism of heat island formation. All factor interactions exhibited a two-factor enhancement effect, and the driving intensity dominated by human activities displayed a dynamic fluctuation pattern: high in 2013, decline in 2018, and rebound in 2024, corresponding to different stages of urban development. (4) The risk detector indicated that NDBI, population density, and land surface temperature were significantly and positively correlated with heat island intensity, while NDVI and elevation were significantly negatively correlated. The warming effect of positive factors was stronger in high-risk areas. This study provides a quantitative scientific basis for optimizing the thermal environment and guiding ecological regulation in Wuhan.*

Keywords— ***Heat Island Effect (UIE), Land Surface Temperature (LST) Inversion, RS and GIS, GeoDetector, Wuhan City***

I. INTRODUCTION

With accelerating urbanization and industrialization, the urban heat island (UHI) effect has increasingly affected urban ecosystems and residents' daily lives, becoming a major concern in urban environmental research (Liang et al., 2010). Meteorologists have recognized that the UHI effect not only influences local meteorological conditions and climate but also contributes to broader climate change in the context of urbanization (Li, 2013). Wuhan, located in the middle and lower reaches of the Yangtze River, experiences prolonged periods of hot weather in summer, when the western Pacific subtropical high frequently dominates regional atmospheric conditions, resulting in abundant sunshine, high temperatures, limited rainfall, and intense solar radiation. When combined with the UHI effect, these climatic conditions can exacerbate the intensity and duration of summer heat, contributing to Wuhan's reputation as a typical "furnace city." In addition, Wuhan is characterized by a dense network of rivers and lakes, diverse land-use types, and heterogeneous underlying surfaces, including plains, hills, built-up areas, woodlands, and water bodies. These characteristics contribute to pronounced spatial variations in the urban thermal environment, making Wuhan a suitable case study for investigating the UHI effect in a large city under specific climatic conditions.

Accordingly, this study investigates Wuhan using remote sensing (RS) and geographic information system (GIS) technologies, integrating Landsat imagery from 2013, 2018, and 2024 with multisource datasets to examine the spatiotemporal patterns and driving mechanisms of the urban thermal environment. Specifically, this study aims to characterize the temporal trends and spatial distribution of LST, assess differences in thermal environmental effects among land-use types, and identify key driving factors using the Geodetector method. By examining both the individual effects of these factors and their interactions, this study seeks to clarify the mechanisms underlying spatial variations in the urban thermal environment and provide a scientific basis for thermal environment assessment and optimization in Wuhan.

II. STUDY AREA AND DATA SOURCES

2.1 Overview of the Study Area

Wuhan is located in eastern Hubei Province, in the middle reaches of the Yangtze River, between 29°58′ and 31°22′ N and 113°41′ and 115°05′ E. The city comprises 13 administrative districts and covers an area of approximately 8,569 km². Located in the eastern Jianghan Plain, Wuhan is characterized by predominantly low-lying, flat terrain, interspersed with a small number of low mountains and hills (Figure 1). The Yangtze River and the Han River flow through the city, which also contains numerous lakes. Water bodies account for approximately one-quarter of the city's total area, earning Wuhan its reputation as the "City of a Hundred Lakes" in China.

Wuhan has a subtropical monsoon climate, with summers frequently influenced by the subtropical high-pressure system, resulting in prolonged periods of high temperatures and hot, humid weather. The annual mean temperature is approximately 16.8°C, while extreme summer temperatures can exceed 40°C and extreme winter temperatures can fall to approximately −10°C. Annual precipitation averages approximately 1,200 mm and is concentrated mainly in summer. As of 2024, Wuhan had a permanent resident population of approximately 13.8 million, with an urbanization rate exceeding 80%. As a major economic, cultural, and transportation hub in central China, Wuhan has experienced rapid urban development in recent years. The continuous expansion of built-up areas, together with the concentration of population and industrial activities in the central urban area, has increased pressure on the urban thermal environment and potentially intensified the urban heat island effect.

International Journal of Environment, Agriculture and Biotechnology
Vol-11, Issue-5; Sep-Oct, 2026
Peer-Reviewed International Journal
Journal Home Page Available: https://ijeab.com/
Journal DOI: 10.22161/ijeab

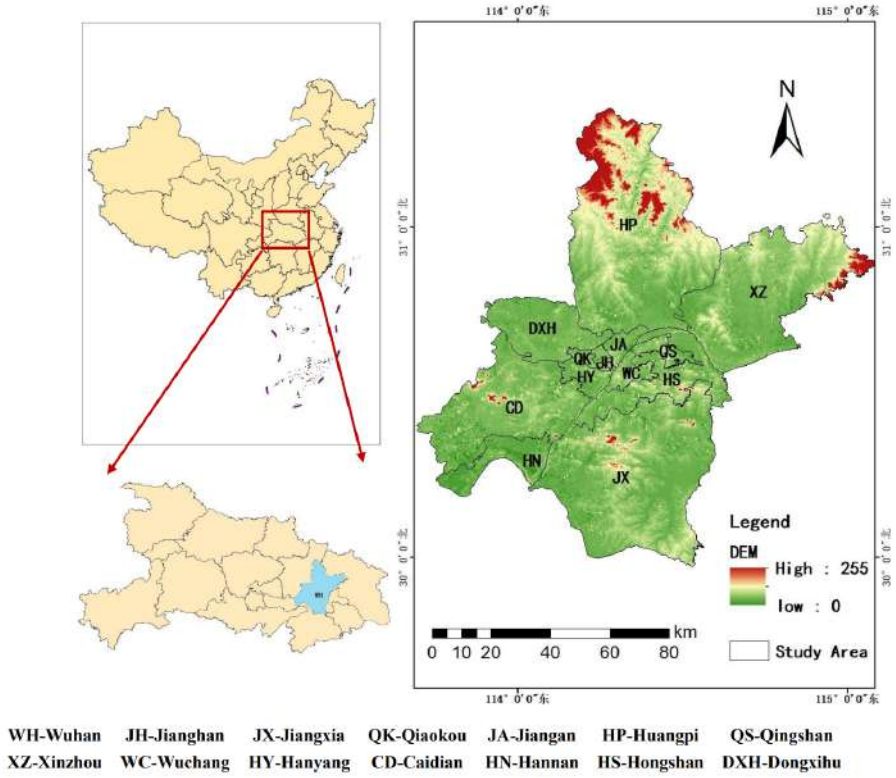


Fig.1 Location and topographic elevation map of Wuhan City

2.2 Data Sources

This study uses multisource datasets for Wuhan for 2013, 2018, and 2024. The data sources and associated preprocessing procedures are described below and summarized in Table 1.

(1) **Administrative boundary data.** Vector data delineating the administrative boundaries of Wuhan's districts were obtained from the National Geomatics Information Public Service Platform. These boundaries define the study area and serve as the spatial reference for data clipping and subsequent spatial analyses.

(2) **Land surface temperature (LST) data.** Landsat Collection 2 Level-2 imagery covering the study area during the summer period (May–August) was obtained through Google Earth Engine (GEE). Cloud-contaminated pixels were masked using the QA_PIXEL quality assessment band, and the appropriate scale factors were applied to convert the original pixel values into physically meaningful measurements. Median compositing was then performed to generate representative imagery for each study year. Where necessary, residual data gaps were filled using observations from adjacent months. The resulting imagery was clipped to the study area boundary, and the thermal and optical bands were exported separately for subsequent analyses.

(3) **Digital elevation model (DEM) data.** DEM data at a spatial resolution of 30 m were obtained from the ASTER Global Digital Elevation Model (ASTER GDEM) dataset through the Geospatial Data Cloud platform. The raster data were clipped to the study area boundary, and the resulting DEM was used for terrain-related analyses.

(4) **Population density (PD) data.** Population density data were obtained from WorldPop's gridded population distribution dataset for China, with a spatial resolution of 1

km. The raster data were clipped to the study area boundary to characterize the spatial distribution of population density and investigate its relationship with the urban thermal environment. Owing to the delayed availability of updated, high-resolution population datasets, a 1-km-resolution population raster based on the latest available census benchmarks was not available for 2024. According to the Wuhan Statistical Yearbook, the city's permanent resident population increased from 12.4477 million in 2020 to 13.8091 million in 2024, while the reported population density increased from 1,453 to 1,611 persons/km². This represents an increase of approximately 10.94% in the total permanent resident population. At the district level, central urban districts, including Jianghan (24,415 persons/km²), Qiaokou (18,727 persons/km²), and Wuchang (13,202 persons/km²), continued to exhibit relatively high population densities, whereas peripheral districts, such as Jiangxia (728 persons/km²) and Xinzhou (640 persons/km²), had substantially lower densities. These figures suggest that the broad spatial contrast between densely populated central districts and less densely populated peripheral districts remained evident during the study period. Accordingly, the 2020 population raster was used as an approximate proxy for the 2024 population distribution. This substitution allows the analysis to retain a spatially explicit representation of population density, although it may not capture population redistribution between 2020 and 2024.

(5) **Vegetation and built-up indices.** The Normalized Difference Vegetation Index (NDVI) and Normalized Difference Built-up Index (NDBI) were derived from Landsat imagery obtained through GEE. These indices were used to characterize vegetation cover and built-up surfaces, respectively, and to examine their relationships with the urban thermal environment.

(6) **Land-use data.** Land-use data were obtained from the China Land Use/Cover Change (CNLUCC) dataset developed by the Resource and Environment Science and Data Center of the Chinese Academy of Sciences. Raster data at a spatial resolution of 1 km were selected to investigate the relationship between land-use patterns and the urban thermal environment. Because data for 2024 were not available in the dataset at the time of analysis, the 2023 land-use dataset was used as a proxy for the 2024 land-surface conditions. This substitution was based on the assumption that broad-scale land-use patterns generally change gradually, although localized changes associated with urban expansion and vegetation loss may occur over shorter periods. The CNLUCC dataset was developed through visual interpretation of Landsat imagery and provides spatial information on major land-use categories, including built-up land, woodland, and water bodies. The 2023 dataset therefore provides a basis for examining the broad spatial relationships between land use and the urban thermal environment near the end of the study period, while potential discrepancies between the 2023 land-use patterns and actual conditions in 2024 should be acknowledged.

Table 1 Data Sources

Number	Data Name	Source and Description
1	Administrative area vector boundary data	Sourced from the National Geomatics Information Public Service Platform （https://www.tianditu.gov.cn）
2	LST	The data is sourced from the Google Earth Engine (GEE) platform. Landsat Level-2 images covering Wuhan City during the summer (May–August) were selected. （https://earthengine.google.com）
3	DEM	From the Geospatial Data Cloud Platform (https://www.gscloud.cn)
4	Population density (PD)	From the WorldPop platform (https://hub.worldpop.org)

5	NDVI	Generated from Landsat image data calculated on the GEE platform (https://earthengine.google.com)
6	NDBI	Generated from Landsat image data calculated on the GEE platform (https://earthengine.google.com)
7	Land use type	Excerpted from the China's Multi-Period Land Use Land Cover Remote Sensing Monitoring Dataset (CNLUCC) data (https://www.resdc.cn/)

III. RESEARCH METHODS

3.1 Technical Workflow

Using Landsat imagery, DEM data, population density data, land-use data, and other relevant datasets for Wuhan, this study follows the technical workflow illustrated in Figure 2. The main procedures are described below.

Step 1. Data Collection and Preprocessing

Multisource datasets for 2013, 2018, and 2024 were collected and preprocessed, including coordinate system transformation, spatial clipping, and cloud masking, as appropriate for each dataset. These procedures ensured a consistent spatial extent and compatible data formats for subsequent analyses. Landsat 8 Collection 2 Level-2 imagery was selected as the primary remote sensing data source. This product provides atmospherically corrected surface reflectance and surface temperature data, subject to the quality and availability of the respective bands.

Step 2. LST Retrieval and Cold- and Hot-Island Classification

The Landsat imagery was processed in ENVI 6.2, including clipping to the study area, application of a vector mask, and the required band-specific preprocessing. The NDVI was calculated from the red and near-infrared bands. Fractional vegetation cover and land surface emissivity were then estimated using the specified methods. LST was retrieved using the single-window algorithm, after which the resulting LST values were classified into cold- and hot-island categories according to the established classification criteria. Spatiotemporal analyses were subsequently conducted at both the city-wide and district levels to examine changes in the proportions of the different thermal categories and identify spatial variations in Wuhan's thermal environment.

Step 3. Extraction of Driving Factors

Five categories of explanatory variables were derived to investigate the factors associated with Wuhan's urban thermal environment: terrain elevation, population density, NDVI, the NDBI, and reclassified land-use categories. These variables represent topographic conditions, human activity intensity, vegetation conditions, built-up surface characteristics, and land-use patterns, respectively.

Step 4. GeoDetector Analysis

The selected explanatory variables were incorporated into the GeoDetector framework to investigate the factors associated with the spatial variation in LST. The factor detector was used to quantify the explanatory power of individual factors, while the interaction detector was applied to assess whether combinations of factors enhanced or weakened their explanatory power. The ecological detector was used to examine whether the effects of different factors differed significantly, and the risk detector was employed to identify differences in LST across the strata of each explanatory variable and to locate areas associated with relatively high temperatures. Together, these analyses were used to identify the dominant factors and their potential interactions in shaping Wuhan's urban thermal environment.

Step 5. Integration of Results

The spatiotemporal patterns of the thermal categories were integrated with the GeoDetector results to characterize the evolution of Wuhan's urban thermal environment and examine its associated driving factors. Based on these findings, targeted recommendations were

formulated to support urban thermal environment management and planning.

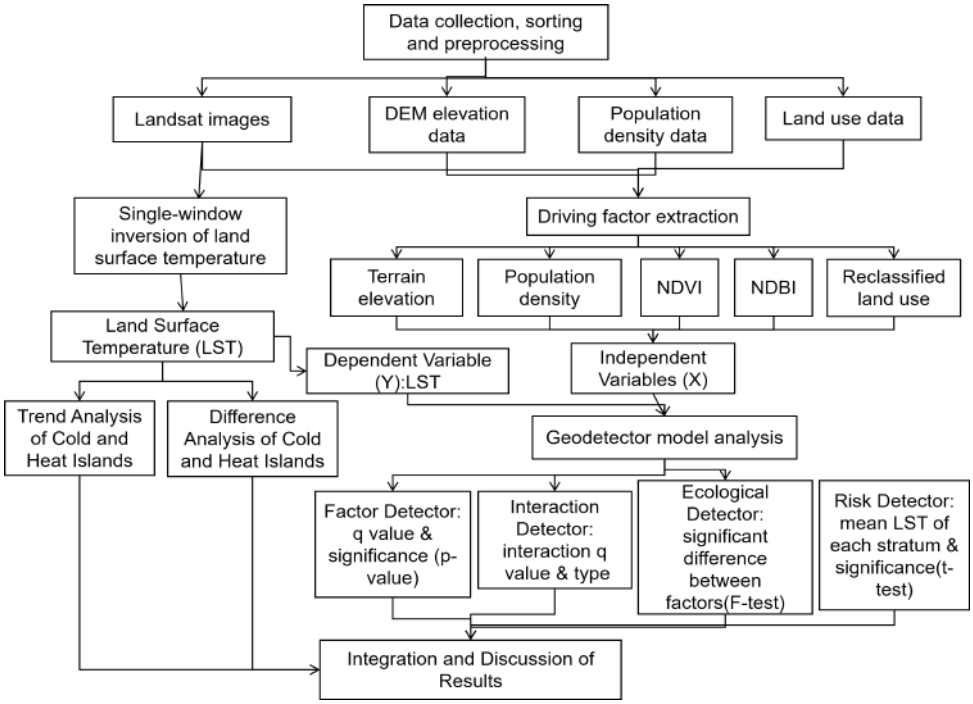


Fig.2 Technical Flowchart

3.2 Heat Island Effect Analysis

3.2.1 Normalized Difference Vegetation Index (NDVI）

NDVI can effectively reflect the surface vegetation coverage, serving as a core indicator to characterize the ecological conditions of the urban underlying surface, and also as the basis for estimating the surface emissivity. The calculation method is as follows in Formula (1):

$$\mathrm{NDVI} = \frac{\rho_{\mathrm{NIR}} - \rho_{\mathrm{RED}}}{\rho_{\mathrm{NIR}} + \rho_{\mathrm{RED}}} \qquad (1)$$

In Equation (1): ρ_{NIR} is the surface reflectance of the near-infrared band of the Landsat L2 product; ρ_{RED} is the surface reflectance of the red band. The NDVI value ranges from [-1, 1], and higher values indicate greater vegetation coverage.

3.2.2 Fractional Vegetation Cover（FVC）

FVC refers to the proportion of the vertical projection area of ground vegetation leaves to the total calculated area (Zhao et al., 2023). The calculation formula for vegetation cover degree (FVC) is constructed based on the pixel binary model and NDVI index (Sheng et al., 2023), as shown in Formula (2):

$$FVC = \frac{NDVI - NDVI_{soil}}{NDVI_{veg} - NDVI_{soil}} \qquad (2)$$

In Equation (2): $NDVI_{soil}$ is the NDVI value of bare soil areas; $NDVI_{veg}$ is the NDVI value of pure vegetation pixels. In this study, cumulative frequencies of 5% and 95% were used as the confidence interval for value selection.

3.2.3 Calculation of Surface Emissivity

Surface emissivity (ε). There is a certain mathematical relationship between surface emissivity and NDVI. When 0.157 ≤ NDVI ≤ 0.727, the calculation process of surface emissivity is as shown in Equation (3).

$$\varepsilon = 1.0094 + 0.047 \times ln(NDVI) \qquad (3)$$

If NDVI > 0.727, the corresponding land surface area is classified as 'fully vegetated area' or 'high-density vegetation area', with ε = 0.986. If NDVI < 0.157, it is either impervious surface or bare soil, which can be further distinguished using the Modified Normalized Difference

Water Index (MNDWI) as shown in Equation (4). A positive result indicates water bodies (ε = 0.995), while a negative result indicates constructed land (ε = 0.970).

$$MNDWI = \frac{p(gre) - p(swir1)}{p(gre) + p(swir1)} \quad (4)$$

In Equation (4), p(gre) represents the reflectance of the green band, and p(swir1) represents the reflectance of the middle infrared band.

This estimation method is the vegetation coverage method for extracting land surface emissivity as a accessories scheme for the single-window algorithm by Sobrino et al. (2004), which is widely used in the study of land surface temperature inversion from Landsat series satellite imagery.

3.2.4 Land Surface Temperature (LST) Retrieval

The land surface temperature (Ts) was retrieved using the single-channel method, and the retrieved results were converted from Kelvin to Celsius (Zhou et al., 2026). Formula (5) is as follows:

$$T_s = \frac{K_2}{\ln\left(\frac{K_1}{L_\lambda} + 1\right)} \quad (5)$$

$$T(℃) = T_S - 273.15$$

In Equation (5): Ts is the surface temperature (K); K_1 and K_2 are satellite calibration constants (Landsat8: K_1=774.89, K_2=1321.08).

3.2.5 Heat Island Classification

To eliminate differences in remote sensing images and land surface temperatures across different times and seasons, enhance comparability between datasets, and avoid the subjective maximum-minimum equal-interval classification method, the mean-standard deviation equal-interval method was adopted (Sui et al., 2024).

$$\bar{T} = \frac{1}{n}\sum_{i=1}^{n} T_i \quad (6)$$

$$\sigma = \sqrt{\frac{1}{n}\sum_{i=1}^{n}(T_i - \bar{T})^2} \quad (7)$$

In Equation (6): $\bar{T}$ is the average land surface temperature of the study area; n is the total number of valid land surface temperature pixels; T*i* is the land surface temperature value of the i-th pixel. In Equation (7): σ is the standard deviation of land surface temperature, representing the degree of spatial dispersion and variation of land surface temperature in the study area.

Based on the land surface temperature inversion results of three periods (2013, 2018, and 2024), the mean and standard deviation of land surface temperature for each year were calculated: in 2013, the mean $\bar{T}$=36.59∘Cand the standard deviation σ=3.54∘C; in 2018, the mean $\bar{T}$=37.60∘C and the standard deviation σ=4.48∘C; in 2024, the mean $\bar{T}$=37.89∘C and the standard deviation σ=4.29∘C. To ensure consistency for interannual comparison, the data from the three periods were integrated and calculated to obtain the overall average $\bar{T}$=37.36∘C and overall standard deviation σ=4.16∘C for the entire study period. Based on this, a unified classification standard was established to divide the study area into five temperature zones (Wang, 2025):

Strong Cold Island Zone：$T < \bar{T} - 1.5\sigma$

Cold Island Zone：$\bar{T} - 1.5\sigma \le T < \bar{T} - 0.5\sigma$

Normal Temperature Zone：$\bar{T} - 0.5\sigma \le T < \bar{T} + 0.5\sigma$

Heat Island Zone：$\bar{T} + 0.5\sigma \le T < \bar{T} + 1.5\sigma$

Strong Heat Island Zone：$T \ge \bar{T} + 1.5\sigma$

3.3 GeoDetector

GeoDetector is a spatial statistical method widely used to investigate spatial stratified heterogeneity and identify factors associated with geographical differentiation. It has two major advantages: first, it can accommodate both numerical and categorical explanatory variables, subject to appropriate data processing; second, it can assess the interaction effects of two factors on a dependent variable (Ma and Ding, 2025). The q-statistic quantifies the extent to which an explanatory variable

accounts for the spatial stratified heterogeneity of the dependent variable. Its underlying principle is based on stratification: the study area is divided into several strata according to the categories or discretized values of an explanatory variable. When the within-stratum variation is lower than the overall variation, the dependent variable exhibits spatial stratified heterogeneity. If the spatial distributions of two variables exhibit a degree of correspondence, their spatial association can be further investigated using GeoDetector.

GeoDetector comprises four components: the factor detector, interaction detector, risk detector, and ecological detector.

1. Factor detector

The factor detector quantifies the spatial stratified heterogeneity of the dependent variable Y and evaluates the explanatory power of an explanatory variable X. It produces a q-statistic, with statistical significance assessed where applicable. A larger q-value indicates that the spatial stratification defined by X accounts for a greater proportion of the spatial stratified heterogeneity of Y. For example, (q = 0.75) indicates that the stratification associated with X accounts for 75% of the spatial stratified heterogeneity of Y, according to the GeoDetector formulation.

2. Interaction detector

The interaction detector assesses whether the combined effect of two explanatory variables, X1 and X2, enhances or weakens their individual explanatory power with respect to Y. Specifically, it calculates the individual q-statistics, q(X1) and q(X2)), and the q-statistic for the overlay strata formed by X1 and X2, denoted as X1∩X2. The interaction type is then identified by comparing the combined q-statistic with the individual q-statistics and their sum.

The five commonly used interaction types are defined as follows:

(1)Nonlinear weakening: q(X1∩X2) < Min(q(X1), q(X2))

(2)Univariate weakening: Min (q(X1), q(X2)) < q(X1∩X2) < Max(q(X1), q(X2))

(3)Bivariate enhancement: q(X1∩X2) > Max(q(X1), q(X2))

(4)Independence: q(X1∩X2) = q(X1) + q(X2)

(5)Nonlinear enhancement: q(X1∩X2) > q(X1) + q(X2)

3. **Risk detector,** used to determine whether there is a statistically significant difference in the mean of the dependent variable Y between different sub-regions (i.e., different categories or partitions). Its statistic is given by Equation (8):

$$t = \frac{\bar{Y}_{h=1} - \bar{Y}_{h=2}}{\left[\frac{V_{ar}(\bar{Y}_{h=1})}{n_{h=1}} + \frac{V_{ar}(\bar{Y}_h = 2)}{n_{h=2}}\right]^{1/2}} \quad (8)$$

where $\bar{Y}_h$ is the mean of sub-region h, n_h is the sample size, and V_{ar} is the variance. This statistic approximately follows a t-distribution. The output results provide significance judgments for pairwise comparisons of sub-region means (e.g., "Y" indicates a significant difference, "N" indicates no significant difference), thereby identifying high-risk or high-value areas.

4. Ecological detector, used to compare whether the impacts of two independent variables X1 and X2 on the spatial distribution of the dependent variable Y are significantly different. The output results are displayed in a matrix format, with rows and columns representing different independent variables. Each cell in the matrix displays "Y" or "N". "Y" indicates that at the 0.05 significance level, the effects of the two independent variables corresponding to that row and column on the spatial distribution of Y are significantly different. "N" indicates no significant difference between the effects of the two independent variables. Its statistic is given by Equation (9):

$$F = \frac{N_{x_1}(N_{x_2} - 1)SSW_{x_1}}{N_{x_2}(N_{x_1} - 1)SSW_{x_2}} \quad (9)$$

where SSW_{X1} and SSW_{X2} are the sums of within-layer variances for the strata formed by x1 and x2, respectively, and N_{X1} and N_{X2} are the sample sizes. If the null hypothesis SSW_{X1}=SSW_{X2} is rejected at a given significance level, it is considered that the effects of the two factors on Y are significantly different. (Wang and Xu, 2017)

IV. RESULTS AND ANALYSIS

4.1 Land Surface Temperature Retrieval and Spatiotemporal Analysis

Based on the LST retrieval results for 2013, 2018, and 2024, a consistent classification scheme was applied to generate heat- and cold-island maps (Figures 3–5). In conjunction with administrative boundary data, the results were analyzed in terms of spatial patterns and temporal evolution to characterize the spatiotemporal dynamics of Wuhan's urban thermal environment.

4.1.1 Spatial Patterns of Heat and Cold Islands

Wuhan's thermal environment exhibited a relatively stable center–periphery pattern. Strong heat-island areas were concentrated in the traditional central urban districts along the Yangtze River and Han River, particularly Hankou, Wuchang, and Hanyang. These areas largely coincided with densely built-up areas and zones of intensive human activity. In contrast, strong cold-island areas were consistently observed near woodland areas in northern Huangpi District, extensive lake systems in southern Jiangxia District, and water bodies within the central urban area, including East Lake. These spatial patterns highlight the cooling role of major ecological land covers in Wuhan's thermal environment.

The main channels of the Yangtze River and Han River also formed prominent linear cooling corridors that spatially separated and moderated heat-island areas along their banks. Together, these urbanized areas, ecological land covers, and major water bodies constituted important structural elements of Wuhan's thermal environment throughout the study period.

4.1.2 Temporal Evolution of Heat and Cold Islands

From 2013 to 2024, heat-island areas expanded outward from the urban core and increased in intensity, whereas cold-island areas decreased overall and became increasingly fragmented.

2013: Strong heat-island areas were concentrated in central urban districts, including Jianghan, Qiaokou, and Wuchang, accounting for 6.1% of the study area. These areas were relatively compact and had clearly defined boundaries. Normal-temperature areas predominated in the suburban zones, while the overall ecological landscape remained relatively intact. In the outer suburbs, particularly Huangpi, Xinzhou, and Caidian, cold-island areas formed relatively extensive and contiguous patches, with clear spatial contrasts between hot and cold zones.

2018: Strong heat-island areas in the central urban area became denser and coalesced into larger patches, with their proportion increasing to 6.7%. Meanwhile, normal-temperature areas declined. Heat-island patches extended beyond the central urban area into nearby suburban districts, including Dongxihu, Hongshan, and Jiangxia. In the outer suburbs, some cold-island areas decreased in extent, and signs of spatial fragmentation became increasingly apparent.

2024: Strong heat-island areas in the central urban area became more spatially continuous, with their proportion increasing markedly to 11.4%. Normal-temperature areas declined substantially. In the near suburbs, individual heat-island patches merged and became increasingly connected to the main urban heat-island belt. Meanwhile, numerous small, localized heat-island patches emerged in built-up areas associated with towns and industrial parks in the outer suburbs, disrupting the previously more contiguous distribution of cold-island areas. The proportion of cold-island areas decreased to 26.6%, accompanied by a marked increase in their spatial dispersion and fragmentation.

Overall, the results indicate that heat-island areas expanded outward from the urban core and intensified between 2013 and 2024, while cold-island areas decreased in extent and became more fragmented. Urban expansion and the associated conversion of natural or semi-natural land covers to artificial surfaces likely contributed to these changes. The spatial evolution of the thermal environment also exhibited a distinct center–periphery gradient: the central urban area was characterized primarily by increasing heat-island intensity, the near suburbs experienced the most pronounced contiguous expansion of heat-island areas, and the outer suburbs showed the

emergence of localized heat-island patches alongside increasing fragmentation of cold-island areas.

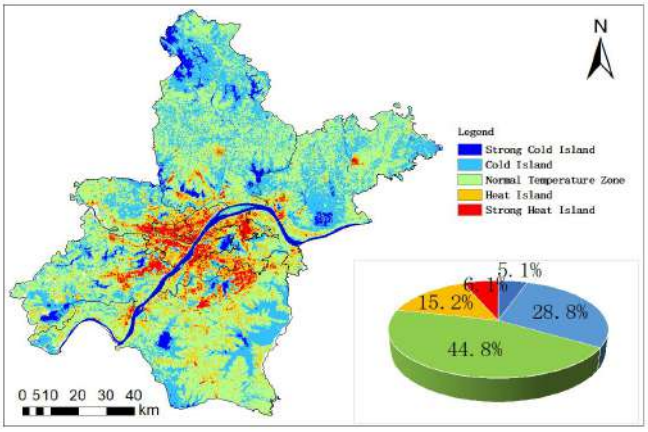


Fig.3 Classification map of heat and cold islands in Wuhan City, 2013

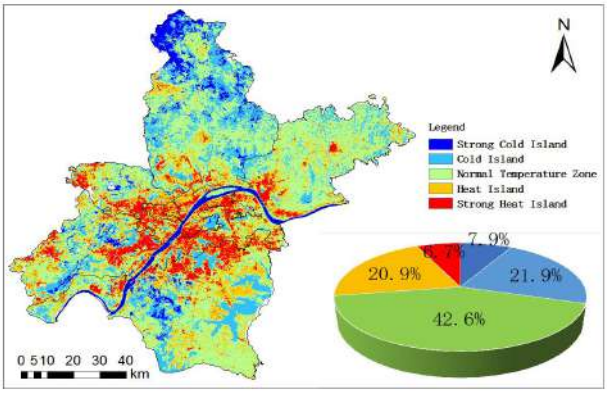


Fig.4 Classification map of heat and cold islands in Wuhan City, 2018

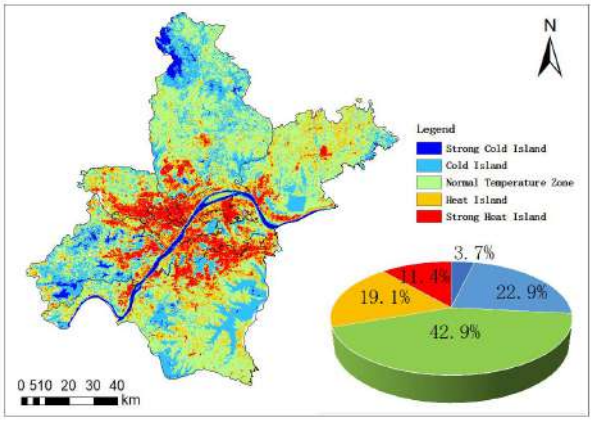


Fig.5 Classification map of heat and cold islands in Wuhan City, 2024

4.1.3 Trends in Heat- and Cold-Island Areas across the Study Region

Based on the LST retrieval results, the proportions of heat-island and cold-island areas were statistically analyzed for each administrative district (Figure 6). The results show that, from 2013 to 2024, the proportion of heat-island areas in Wuhan increased from 43.98% to 54.17%, representing a rise of 10.19 percentage points. Linear regression analysis revealed a strong positive temporal trend ($R^2 = 0.9146$). In contrast, the proportion of cold-island areas decreased from 24.81% to 19.96%, a decline of 4.85 percentage points. This decrease was most pronounced between 2013 and 2018, after which the declining trend became less pronounced. Overall, heat-island areas exhibited a clear increasing trend, whereas cold-island areas showed a decreasing trend ($R^2 = 0.6754$). These findings quantitatively support the observed expansion and increasing aggregation of heat-island areas, alongside the overall contraction and fragmentation of cold-island areas.

This pattern suggests deterioration in Wuhan's urban thermal environment associated with the increasing artificialization of land surfaces. The opposing trends in heat-island and cold-island areas further suggest that the encroachment of urban development on ecological spaces, particularly green spaces and water bodies, may have contributed to the intensification of the urban heat-island effect in Wuhan.

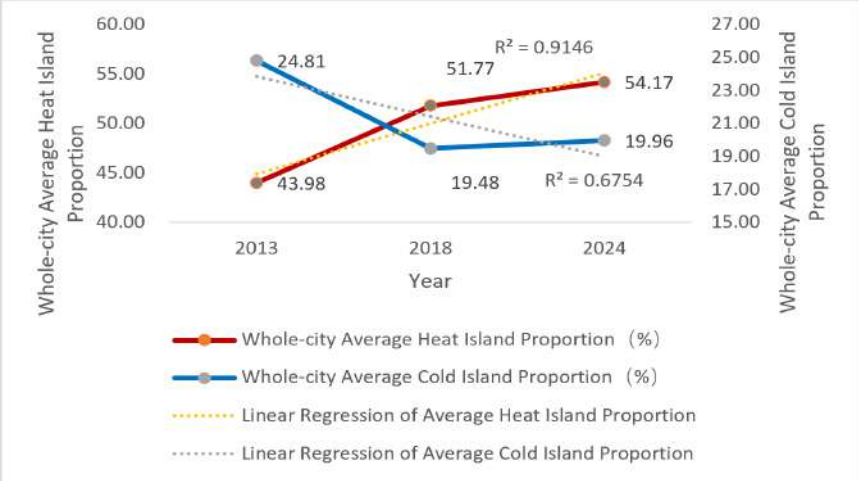


Fig.6 Trends in the areal proportion of heat islands and cold islands, 2013–2024

Pronounced spatial differences in the proportion of heat-island areas were observed among Wuhan's administrative districts, exhibiting a distinct spatial gradient characterized by higher proportions in the central urban area and lower proportions in the outer suburban areas (Figure 7). In 2024, the proportions of heat-island areas in Jianghan and Qiaokou districts both exceeded 90%, indicating that these districts were among the areas most severely affected by the urban heat-island effect. In contrast, the corresponding proportions in Huangpi and Xinzhou districts were below 30%, substantially lower than those in the central urban area.

From 2013 to 2024, the proportion of heat-island areas increased in all administrative districts, although the magnitude of the increase varied considerably across the urban–suburban gradient. Hongshan and Dongxihu districts exhibited the most pronounced increases, suggesting that the near suburbs have become key areas of urban warming associated with outward urban expansion. In the central districts of Jianghan and Qiaokou, where urban development is relatively mature and built-up areas are highly concentrated, the proportions of heat-island areas remained consistently high, with comparatively modest increases over the study period. Extensive commercial and residential development, dense road networks, and impervious surfaces, combined with multiple sources of anthropogenic heat, may contribute to the persistently high heat-island proportions in these districts.

In Qingshan District, the concentration of heavy industry, particularly the Wuhan Iron and Steel Corporation, provides a potential source of sustained anthropogenic heat emissions that may contribute to the gradual intensification of the local heat-island effect. Meanwhile, Hongshan District, particularly the Optics Valley area, and Hanyang District, including the Zhuankou Economic and Technological Development Zone, have experienced continued expansion of industrial parks and residential areas over the past decade. The rapid expansion of impervious surfaces in these areas may have contributed substantially to the increase in the proportion of heat-island areas. In outer suburban districts such as Huangpi and Jiangxia, new-town development and associated land-use changes, including the conversion of farmland and small water bodies to built-up land, may also have contributed to the expansion of heat-island areas. In Caidian District, ecological protection and development restrictions around Houguan Lake may have helped limit the increase in heat-island areas by preserving the lake's cooling function and surrounding ecological spaces.

Overall, the spatial distribution of heat-island areas in Wuhan closely corresponds to the distribution of built-up land. The extensive impervious surfaces and concentrated human activities in the central urban area are likely to be

important factors associated with the prevalence of heat-island conditions, while continued urban expansion in the suburbs may be contributing to the outward spread of heat-island areas.

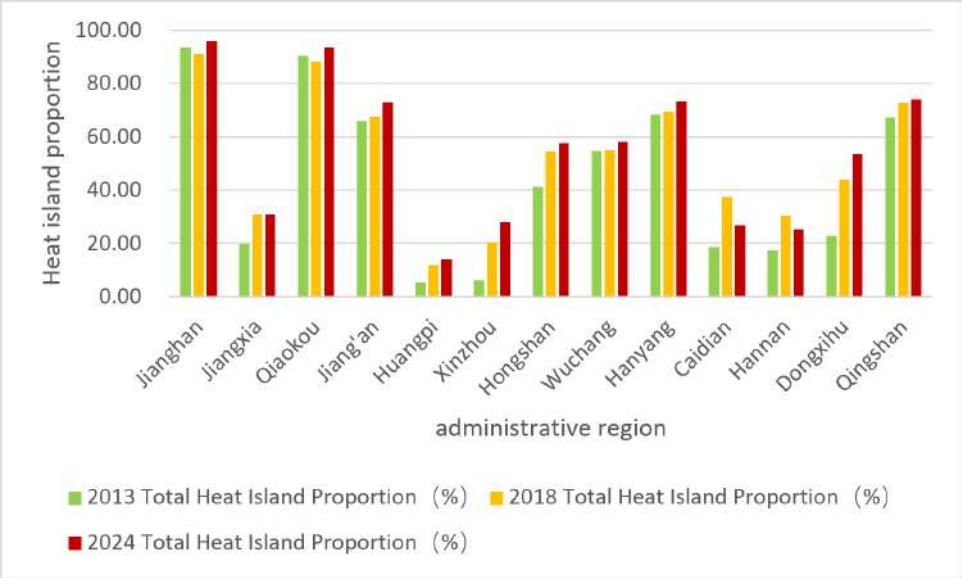


Fig.7 Changes in the proportion of heat islands in each administrative region, 2013–2024

The spatial distribution of cold-island areas in Wuhan exhibits a pattern of concentration in the outer suburbs and scarcity in the central urban area, contrasting markedly with the distribution of heat-island areas (Figure 8). In 2024, the proportions of cold-island areas in Huangpi and Jiangxia districts exceeded 20%, identifying them as major cold-island zones. In contrast, the corresponding proportions in Jianghan and Qiaokou districts were below 5%, indicating a severe scarcity of cooling spaces. In the older inner-city areas, the historical infilling of rivers and lakes, the high proportion of impervious surfaces, and the scarcity of large, contiguous green spaces have limited the availability of cooling areas. Dense street networks may also impede ventilation, while anthropogenic heat from commercial, residential, and industrial activities further intensifies local thermal stress. Moreover, the high degree of built-up development restricts opportunities to establish large-scale blue–green spaces (Li et al., 2026).

From 2013 to 2024, the proportion of cold-island areas declined in most administrative districts, with particularly pronounced decreases in Huangpi and Jiangxia. Despite their extensive natural woodlands, agricultural land, and lakes, including Tangxun Lake, these districts have experienced rapid urbanization. Encroachment on lakeside buffer zones and small suburban water bodies has fragmented contiguous blue–green spaces, contributing to the substantial contraction of cold-island areas (Ren, 2024). These changes suggest that urban expansion has placed considerable pressure on suburban cooling spaces, weakening their thermal-regulation functions. In Hongshan and Hanyang districts, large water bodies such as East Lake and Moshui Lake remain important cooling resources; however, continued encroachment of built-up land on surrounding green spaces may have reduced the extent of their cooling influence, contributing to the gradual decline in cold-island areas. By contrast, ecological conservation and lakeside restoration around Houguan Lake in Caidian District have supported the recovery of ecological land, accompanied by an increase in the proportion of cold-island areas. Overall, the spatial and temporal contraction of cold-island areas broadly coincides with the intensification of the urban heat-island effect, suggesting that the loss of cooling spaces may have contributed to the deterioration of Wuhan's urban thermal environment.

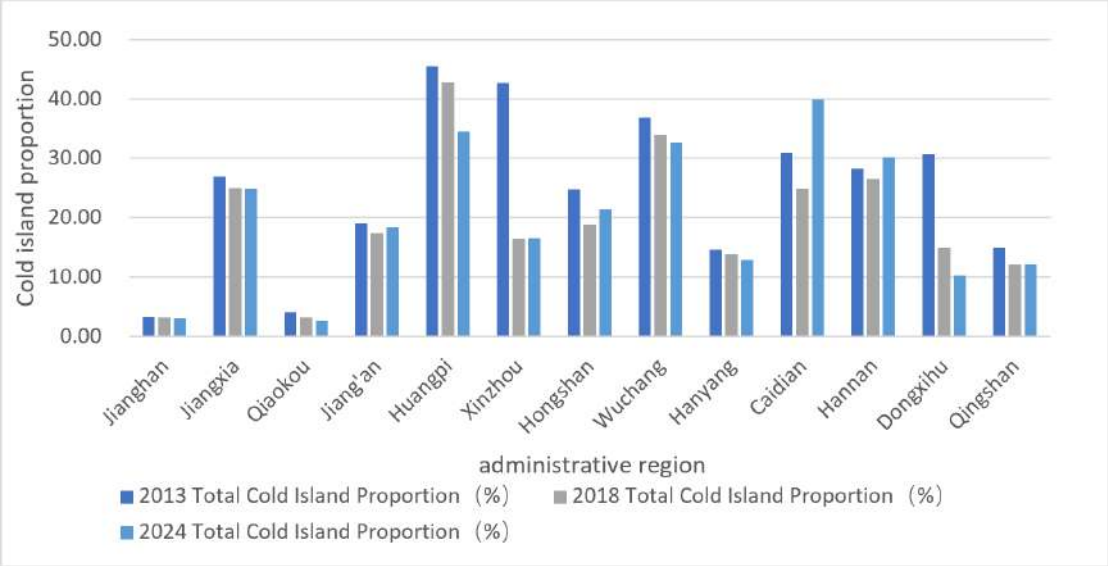


Fig.8 Changes in the proportion of cold islands in each administrative region, 2013–2024

The combined analysis of spatial imagery and administrative-district proportions reveals distinct zonal gradients in the evolution of urban heat and cold islands. Development in the central urban core has largely reached saturation, leaving limited scope for large-scale outward expansion. Consequently, changes in this zone are characterized primarily by increasing heat island intensity and the continued contraction of internal cold-island patches. The overall heat–cold island configuration remains relatively stable, although urban renewal contributes to localized warming. The inner suburbs constitute the principal zone of urban expansion and heat island growth, experiencing the most rapid urbanization and industrialization. The substantial increase in impervious surface coverage has led to a sharp decline in cold islands and the contiguous expansion of heat islands, making this zone the most dynamic in terms of thermal landscape change. In the outer urban districts, cold islands remain the dominant landscape component. However, industrial spillover, transportation infrastructure development, and township expansion have driven the emergence of isolated heat islands and their localized spread, indicating a later stage of thermal landscape transformation. Meanwhile, contiguous cold-island areas have gradually fragmented into scattered patches.

Overall, heat island expansion in Wuhan from 2013 to 2024 followed a clear spatial gradient of inner suburbs > outer urban districts > central urban core, closely corresponding to the city's concentric urban expansion pattern. In contrast, cold-island areas generally exhibited contraction and fragmentation, particularly in the inner and outer suburbs. The persistent loss of cold islands has not only weakened regional ecological regulation capacity but also exacerbated intra-urban thermal environmental disparities. These spatiotemporal patterns provide an empirical basis for further investigating the relationship between urban spatial structure and thermal environmental effects, as well as for developing targeted ecological planning strategies.

4.2 Driving Factors of the Urban Heat Island Effect

4.2.1 Factor Detector Results

The factor detector was used to quantify the independent explanatory power (q-value) of each driving factor for the spatial differentiation of the urban heat island effect. The results showed that, in 2013, the factors ranked in descending order of explanatory power were NDBI > NDVI > population density > land use type > elevation. NDBI exhibited the highest q-value, indicating that it was the dominant independent explanatory factor for the urban heat island effect in that year. This finding suggests that

the expansion of built-up areas played a critical role in shaping the spatial variation in land surface temperature (LST). NDVI ranked second, highlighting the significant role of vegetation cover in regulating LST. Population density and land use type demonstrated moderate explanatory power, whereas elevation had an extremely low q-value, suggesting limited independent explanatory power for the spatial differentiation of the heat island effect (Figure 9).

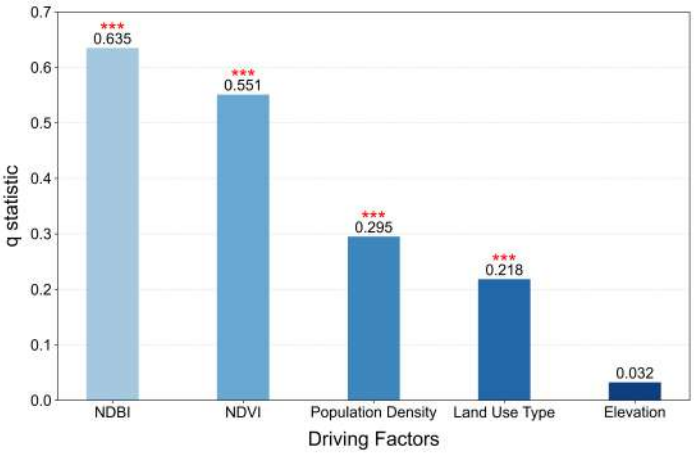


Fig.9 Results of the factor detector in 2013

*** indicates significance at the $p < 0.001$ level

In 2018, the independent explanatory power of all driving factors decreased substantially compared with 2013. The factors ranked in descending order of q-values were NDBI > NDVI > land use type > population density > elevation. NDBI and NDVI remained the two most influential factors in terms of explanatory power, although their q-values decreased by 0.190 and 0.135, respectively, relative to 2013. These declines may reflect, in part, the effects of urban ecological restoration and green space development, which may have altered the relationships between built-up land, vegetation cover, and the spatial differentiation of the heat island effect. The explanatory power of land use type and population density also declined, indicating their limited independent explanatory capacity. The q-value for elevation increased slightly to 0.054 but remained substantially lower than those of the other factors, suggesting that elevation had limited independent explanatory power for the spatial differentiation of the heat island effect (Figure 10)

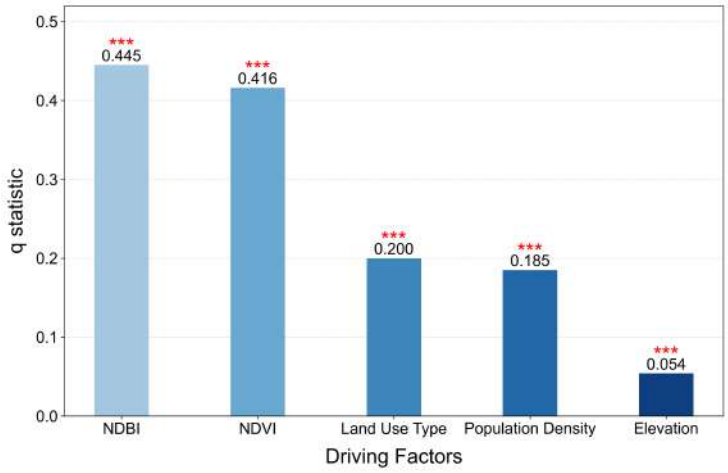


Fig.10 Results of the factor detector in 2018

*** indicates significance at the $p < 0.001$ level

In 2024, the independent explanatory power of the driving factors rebounded compared with 2018. The factors ranked in descending order of q-values were NDBI > NDVI > land use type > population density > elevation. The q-values of NDBI (0.528) and NDVI (0.451) increased markedly relative to 2018, with NDBI exhibiting the greater increase. This suggests that accelerating urban development may have strengthened the independent explanatory power of built-up land expansion for the spatial differentiation of the heat island effect. The q-values of land use type (0.296) and population density (0.248) also increased substantially, indicating a potential strengthening of the associations between human activities, land use patterns, and the heat island effect. In contrast, the q-value of elevation declined to 0.027, the lowest level observed over the three study years, indicating that elevation had consistently limited independent explanatory power for the spatial differentiation of the heat island effect (Figure 11).

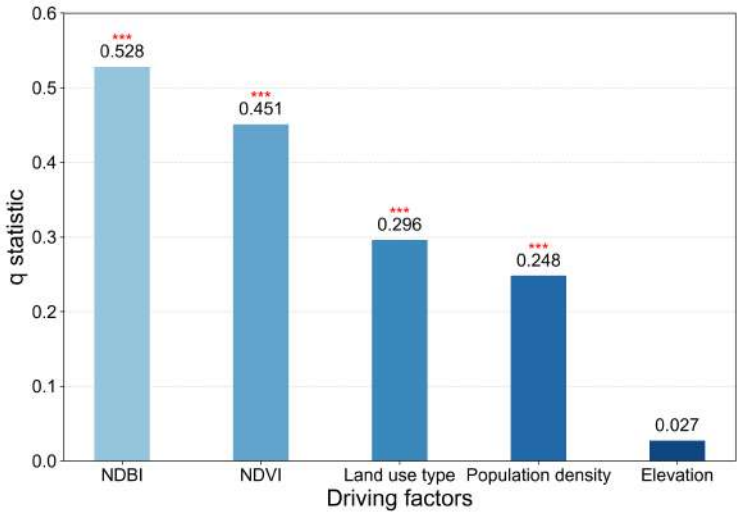


Fig.11 Results of the factor detector in 2024

*** indicates significance at the $p < 0.001$ level

The comprehensive factor detection results indicate that NDBI consistently exhibited the highest explanatory power from 2013 to 2024, followed by NDVI. The q-values of these two factors were substantially higher than those of the other factors, suggesting that built-up land expansion and changes in vegetation cover were the primary independent explanatory factors associated with the urban heat island effect in Wuhan. Overall, the q-values of the driving factors followed a pattern of decline from 2013 to 2018, followed by a rebound in 2024. This temporal variation may reflect the changing influences of urban development and ecological regulation measures across different stages of urbanization. The q-value of elevation remained below 0.06 in all three study years, indicating limited independent explanatory power for the spatial differentiation of the heat island effect. Furthermore, anthropogenic factors, including NDBI, NDVI, population density, and land use type, generally exhibited greater explanatory power than elevation, highlighting the prominent role of human activities in shaping Wuhan's urban heat island

4.2.2 Interaction Detector Results

Interaction detection examines whether the combined effects of two driving factors enhance or weaken their explanatory power for the spatial differentiation of the dependent variable (Chen and Zhong, 2024). The results show that, from 2013 to 2024, all pairs of driving factors exhibited two-factor enhancement, with neither independent nor nonlinear weakening detected. The explanatory power of factor interactions was consistently greater than that of individual factors, highlighting the importance of multifactor interactions in explaining the spatial differentiation of the urban heat island effect. The

interaction patterns varied across the study years, reflecting potential changes associated with different stages of urban development.

In 2013, the q-values of factor interactions ranged from 0.032 to 0.771, representing the highest overall interaction strength among the three study years. The interaction between NDBI and NDVI exhibited the highest explanatory power (q = 0.771), suggesting that the combined effects of built-up land expansion and vegetation cover changes were closely associated with the spatial differentiation of the heat island effect. Furthermore, the interactions between NDBI and population density (q = 0.674), NDBI and land use type (q = 0.679), and NDVI and population density (q = 0.661) all had q-values exceeding 0.65. These results highlight the strong combined explanatory power of urban development intensity, population distribution, and land surface characteristics. By contrast, elevation exhibited relatively low explanatory power both independently and in interaction with other factors, indicating its limited contribution to explaining the spatial differentiation of the heat island effect (Figure 12).

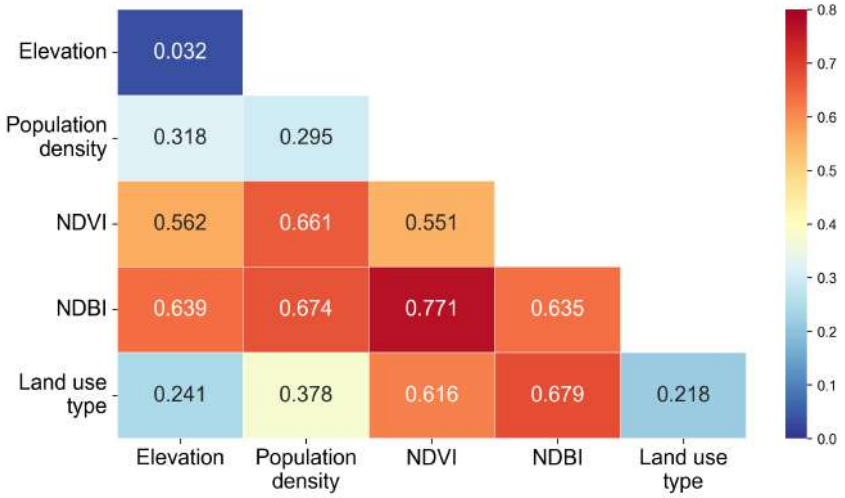


Fig.12 Heatmap of the interaction detector results for LST driving factors in 2013

In 2018, the q-values of factor interactions ranged from 0.054 to 0.593, indicating an overall decline in interaction strength compared with 2013. Although the interaction between NDBI and NDVI remained the strongest (q = 0.593), its q-value decreased by 0.178 relative to 2013. This decline may be associated with the implementation of ecological management measures, including urban green space development, which may have moderated the combined effects of built-up land expansion and vegetation cover changes on the urban heat island effect. Meanwhile, the interactions between NDBI and land use type (q = 0.501) and between NDVI and population density (q = 0.493) continued to exhibit relatively high explanatory power. These results highlight the persistent importance of interactions among urban development, population distribution, and land surface characteristics in explaining the spatial differentiation of the heat island effect. By contrast, elevation-related effects remained relatively weak (Figure 13).

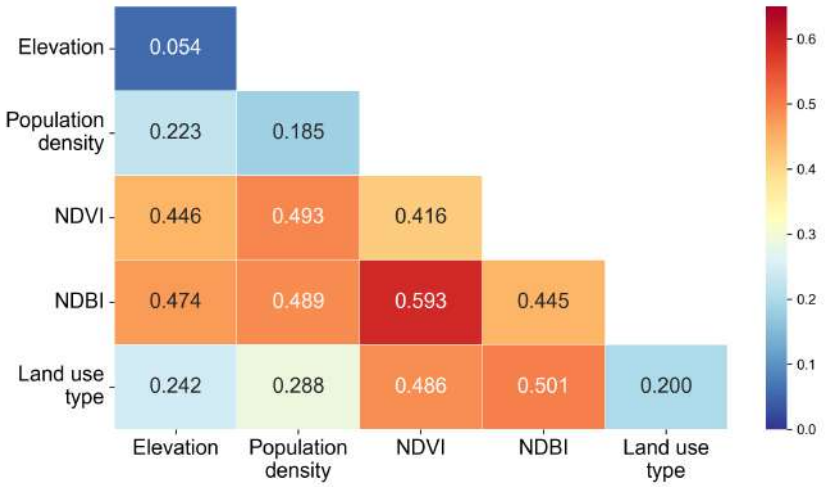


Fig.13 Heatmap of the interaction detector results for LST driving factors in 2018

In 2024, the q-values of factor interactions ranged from 0.027 to 0.674, indicating an overall rebound in interaction strength compared with 2018. The interaction between NDBI and NDVI remained dominant (q = 0.674), increasing by 0.081 relative to 2018. This increase may reflect the renewed intensification of competition between built-up land expansion and vegetation space amid accelerated urban development. Meanwhile, the q-values for the interactions between NDBI and population density (q = 0.594) and between NDBI and land use type (q = 0.613) also increased substantially, highlighting the combined explanatory power of human activity intensity and built-up land expansion. By contrast, the independent explanatory power of elevation reached its lowest level over the three study years, while its interactions with other factors remained relatively weak (Figure 14).

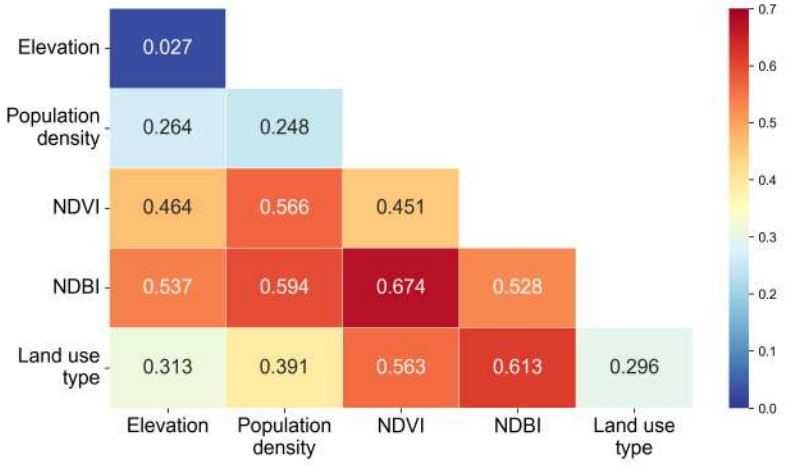


Fig.14 Heatmap of the interaction detector results for LST driving factors in 2024

The comprehensive interaction detection results for the three study years indicate that the interaction between NDBI and NDVI consistently exhibited the highest explanatory power from 2013 to 2024, highlighting the importance of the combined effects of built-up land expansion and vegetation cover changes in shaping Wuhan's urban heat island patterns. The interaction strength followed a pattern of high values in 2013, a decline in 2018, and a rebound in 2024. This temporal variation may be associated with changes in urban development and ecological management measures. All factor pairs exhibited two-factor enhancement, indicating

that the spatial differentiation of the heat island effect is better explained by interactions among multiple factors than by individual factors alone. In contrast, the independent and interactive explanatory power of elevation remained consistently low, suggesting that it was not a dominant factor in explaining the spatial differentiation of Wuhan's urban heat island effect.

4.2.3 Results of the Ecological Detector

The ecological detector was used to assess whether significant differences existed between the effects of different driving factors on the spatial differentiation of the urban heat island effect. The results are summarized as follows.

In 2013, all pairs of driving factors exhibited significant differences (Y), with no nonsignificant pairs identified. This indicates that the effects of elevation, population density, NDVI, NDBI, and land use type differed significantly in their explanatory power for the spatial differentiation of the heat island effect.

In 2018, significant differences persisted for most factor pairs (Y), whereas the pair of population density and land use type showed no significant difference (N). This result suggests that these two factors had statistically indistinguishable effects on the spatial differentiation of the heat island effect during this period. The remaining factor pairs continued to exhibit significant differences, indicating that their relative explanatory effects remained distinguishable.

In 2024, all pairs of driving factors again exhibited significant differences (Y), with no nonsignificant pairs identified. This suggests that the effects of population density and land use type became statistically distinguishable again. Overall, the ecological detector results reveal temporal variation in the differences between the explanatory effects of individual factors, with only population density and land use type showing no significant difference in 2018 (Figure 15).

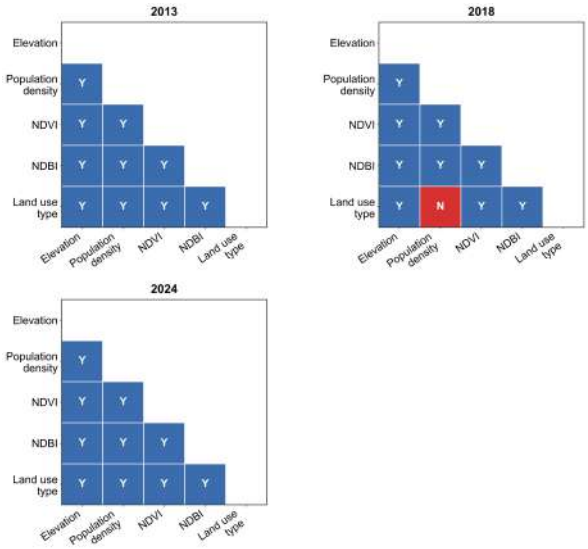


Fig.15 Results of the Ecological Detector for 2013, 2018, and 2024

Overall, from 2013 to 2024, the differences in the effects of most factors were significant, indicating that the driving factors of the urban heat island effect in Wuhan had differentiated influence mechanisms overall, with no universal substitutable relationship. The periodic convergence of population density and land use type in 2018 may be related to the coordinated adjustment of urban population distribution and land use structure during that period. From the perspective of long-term evolution trends, the differences in the effects of various driving factors remained predominantly significant, suggesting that different factors play irreplaceable roles in the formation of the urban heat island effect.

4.2.4 Results of the Risk Detector

The risk detector was used to examine the gradient differentiation in the effects of various driving factors on the UHI effect by comparing LST across different risk levels (Figures 16–18).

NDBI was positively associated with LST. Mean LST increased progressively with increasing NDBI risk levels. The boxplots exhibited a clear stepwise increase, with limited overlap between boxes, indicating pronounced temperature differences across risk levels. The largest temperature increase occurred at high-risk levels, and LST in Level 5 areas in 2024 was notably higher than in the previous two periods. These findings suggest that the association between built-up land and elevated LST was particularly pronounced in high-risk areas and became stronger over time.

NDVI was negatively associated with LST. The boxplots showed a clear downward trend across NDVI levels, indicating the cooling effect associated with greater vegetation cover. LST was lowest in low-risk areas, with a particularly evident cooling pattern in low-to-moderate-risk areas.

Population density was positively associated with LST, which increased with rising risk levels. However, substantial overlap between the boxes at Levels 4 and 5 suggests that temperature differences became less distinct at higher population-density levels. The temperature response was more evident at moderate-to-high risk levels, while LST in high-risk areas was higher in 2024 than in the previous two periods. This pattern indicates a stronger association between population density and elevated LST in high-risk areas.

Land use type was positively associated with LST. Areas dominated by built-up land exhibited the highest temperatures and heat island risk. However, considerable overlap among the boxes indicates substantial within-category heterogeneity, potentially reflecting differences in vegetation cover, building density, and other local characteristics.

Elevation was negatively associated with LST. Mean LST declined progressively across increasing elevation-related risk levels, highlighting the role of topography in spatial variations in the thermal environment. This pattern remained consistent across all three periods, suggesting a persistent association between elevation and lower LST.

Overall, NDBI, population density, and land use type were positively associated with LST, whereas NDVI and elevation were negatively associated with it. The relationships varied across risk levels: positive associations were more pronounced in high-risk areas, while the cooling association of vegetation was particularly evident in low-to-moderate-risk areas. From 2013 to 2024, the association between NDBI and elevated LST strengthened, whereas the cooling association of NDVI remained relatively stable. These findings highlight the importance of managing built-up land expansion and maintaining vegetation cover in mitigating Wuhan's UHI effect.

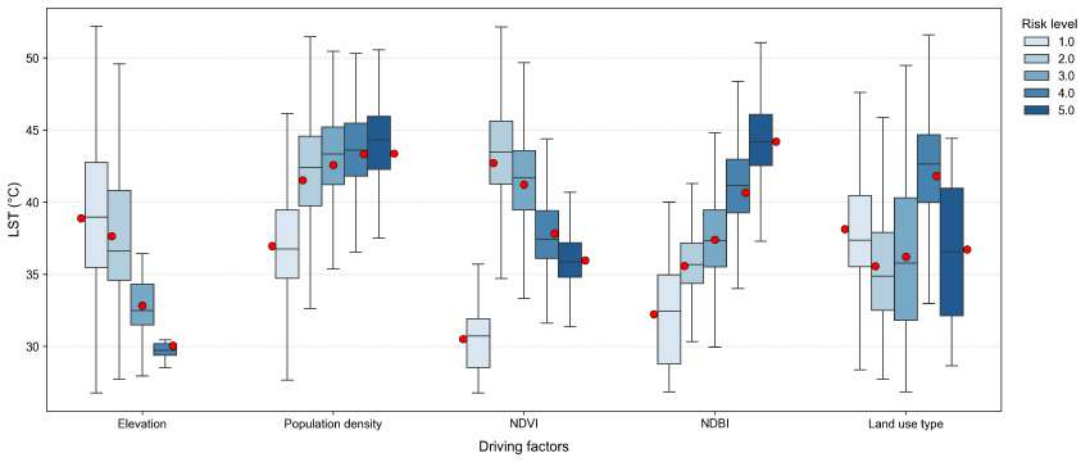


Fig.16 Risk detector results for the factors influencing LST in 2013

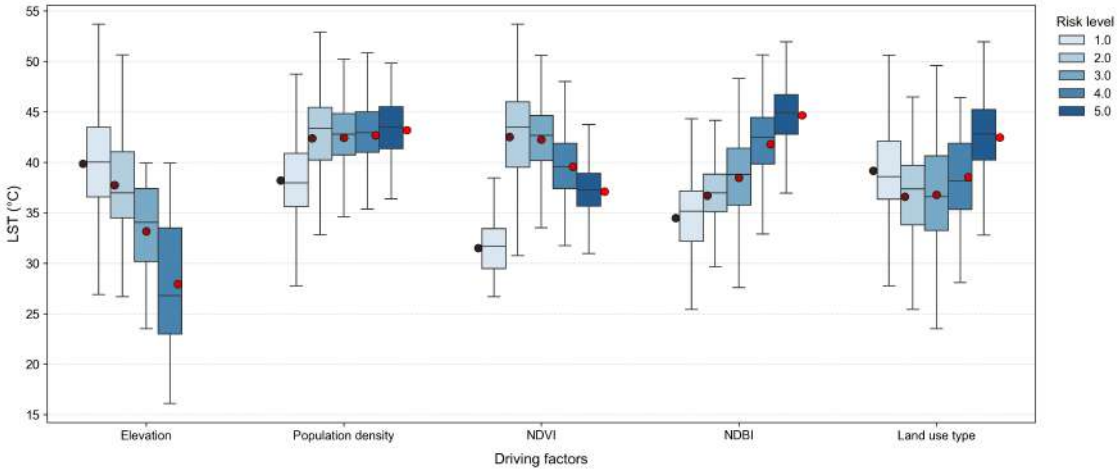


Fig.17 Risk detector results for the factors influencing LST in 2018

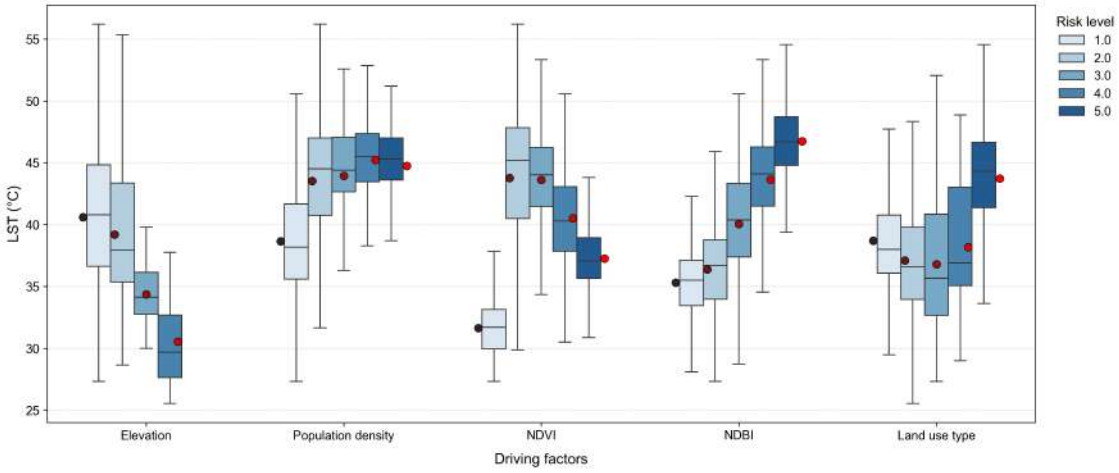


Fig.18 Risk detector results for the factors influencing LST in 2024

The UHI effect in Wuhan reflects the combined influence of human activities and multiple interacting factors. The trade-off between built-up land expansion and vegetation degradation represents a key tension in its long-term evolution. From 2013 to 2024, NDBI and NDVI exhibited the strongest interaction in explaining UHI spatial differentiation. The interaction intensity fluctuated over time, whereas topographic influence remained relatively weak. All factor pairs exhibited two-factor enhancement, with no independent effects detected. Ecological detection revealed significant differences in explanatory power between most factor pairs, except for population density and land use type in 2018. Risk detection further indicated that built-up land expansion and population agglomeration were associated with higher LST, whereas vegetation cover and elevation were associated with lower LST.

Accordingly, the following measures are recommended: (1) control disorderly urban expansion, promote compact development, and limit the warming associated with built-up land; (2) increase urban vegetation cover, establish ventilation corridors and ecological buffer zones, and strengthen vegetation-related cooling; (3) alleviate population pressure in urban cores and improve the equitable distribution of public services; and (4) prioritize high-risk areas through measures such as permeable pavements and green buildings, while protecting ecological resources in low-risk areas.

V. CONCLUSION

This study investigated the spatiotemporal evolution of the UHI effect in Wuhan in 2013, 2018, and 2024 using Landsat imagery and multisource auxiliary data. LST was retrieved and analyzed, and the geographical detector model was employed to examine the factors associated with its spatial differentiation. The main conclusions are as follows.

(1) From 2013 to 2024, the UHI effect in Wuhan intensified, exhibiting a broadly concentric spatial pattern characterized by strong heat islands in the urban core and shrinking cold-island areas toward the periphery. The proportion of heat-island areas increased from 43.98% to 54.17%, while that of cold-island areas declined from 24.81% to 19.96%. Strong heat islands formed contiguous patches in the central urban area, while the most pronounced expansion occurred in the inner suburbs. Cold-island areas in the outer suburbs became increasingly fragmented, indicating outward diffusion of the UHI effect from the urban core toward the inner suburbs.

(2) Underlying surface characteristics were strongly associated with UHI differentiation. NDBI and NDVI consistently exhibited the highest single-factor explanatory power, highlighting the importance of built-up land and vegetation cover. Population density and land use type had comparatively weaker explanatory power, while elevation had the weakest influence. These findings underscore the importance of urban development and vegetation changes in shaping the spatial distribution of LST.

(3) Interactions among all examined factors enhanced their explanatory power, indicating a synergistic pattern of influence involving anthropogenic and natural factors. The NDBI–NDVI interaction had the strongest explanatory power, highlighting the combined relevance of built-up land expansion and vegetation conditions to UHI differentiation. Land use types also exhibited contrasting thermal characteristics: built-up and industrial areas were associated with higher temperatures, whereas forests and water bodies generally provided cooler environments.

(4) UHI evolution was closely associated with urban expansion, industrial development, and changes in ecological land. Extensive impervious surfaces in the central urban area were associated with persistent strong heat islands, while expansion in the outer suburbs may be linked to new-town development, transport infrastructure, and agricultural land conversion. Vegetation cover, urban green spaces, and water bodies played important roles in moderating local temperatures. These findings suggest that UHI mitigation requires an integrated approach, including increasing vegetation cover in built-up areas, protecting wetlands and other ecological spaces, and establishing ecological green corridors between major heat-island clusters to limit their further coalescence (Wang and Gao, 2026).

REFERENCES

[1] Liang, Y., Chen, Z., and Xia, Z. Decadal Evolution and Mechanism of the Urban Heat Island Effect in Wuhan Based on RS and GIS. Resources and Environment in the Yangtze Basin, 2010, 19(08): 914-918.

[2] Li, A. Remote Sensing Analysis of Urban Heat Island Effect in Mianyang City Based on RS. Anhui Agricultural Science Bulletin, 2013, 19(13): 143-148. DOI: 10.16377/j.cnki.issn1007-7731.2013.13.010.

[3] Ma, X., and Ding, H. Study on Spatiotemporal Evolution Characteristics and Driving Mechanism of Thermal Environment in Historical Urban Areas: A Case of Ming City Wall Area in Xi'an. In: China Urban Planning Society, Shenyang Municipal People's Government. Toward Chinese-Style Modernization: Value and Action of Planning—Proceedings of 2025 China Annual Conference on Urban Planning (09 Urban Ecological Planning). School of Architecture, Chang'an University, 2025: 666-680. DOI: 10.26914/c.cnkihy.2025.046698.

[4] Wang, Z. X., and Gao, W. Analysis of Heat Island Effect in Tianjin Based on Surface Temperature Inversion and Geodetector Model. Journal of Atmospheric and Environmental Optics, 2026, 21(02): 330-342.

[5] Zhao, Q., Tan, L., Fang, Q. S., et al. Analysis of Spatiotemporal Evolution and Influencing Factors of Heat Island Effect in Hefei Based on Satellite Data. Journal of Atmospheric and Environmental Optics, 2023, 18(02): 153-167.

[6] Sui, J. M., Jia, G. M., Tian, N., et al. Analysis on Change and Influencing Factors of Urban Heat Island Effect in Baoding Based on Landsat Images. Inner Mongolia Science Technology & Economy, 2024, (13): 101-104+109.

[7] Sheng, L. L., Hao, S., Cui, Y. H., et al. Influence of Urban Development on Surface Heat Island Effect and Its Relationship: A Case of Hefei and Nanchang. Journal of Atmospheric and Environmental Optics, 2023, 18(06): 602-616.

[8] Wang, J. F., and Xu, C. D. Geodetector: Principle and Prospective. Acta Geographica Sinica, 2017, 72(01): 116-134.

[9] Wang, Y. N. Research on Urban Heat Island Effect Analysis Based on Remote Sensing Images. Geomatics & Spatial Information Technology, 2025, 48(05): 75-77.

[10] Zhou, X. S., Zhang, Y. S., and Huang, Q. H. Study on Factors of Urban Local Climate Zone Heat Island Intensity Based on Geodetector. Journal of Hebei Normal University (Natural Science Edition): 1-17. https://doi.org/10.13763/j.cnki.jhebnu.nse.202605001.

[11] Chen, P. H., and Zhong, K. W. The Impact of Urban Land Use Changes on the Urban Heat Island Effect: A Case Study of Nanjing. Science of Surveying and Mapping, 2024, 49(07): 173-183. DOI: 10.16251/j.cnki.1009-2307.2024.07.018.

[12] Li, Q.Q., Li, M., and Liu, H.M. Comparison of Methods for Exploring Spatiotemporal Variations of Urban Heat Island Effect: With Wuhan Metropolitan Development Area as an Example. Chinese Journal of Applied Ecology, vol. 37, no. 3, 2026, pp. 671–682.

[13] Ren, L. Spatiotemporal variation of urban water bodies and its impact on thermal environment in Wuhan, China. Hubei University, 2024. DOI:10.27130/d.cnki.ghubu.2024.000608.

[14] Sobrino, J.A., Jimenez-Munoz, J.C. and Paolini, L. Land Surface Temperature Retrieval from LANDSAT TM 5. Remote Sensing of Environment, 90, 2024, 434-440. http://dx.doi.org/10.1016/j.rse.2004.02.003